# Supplementary Materials for

## In situ acoustic manufacturing of conformal brain–computer interfaces

Shuangquan Gou[1], Peikun Mo[2], Wenliang Liu[3], Rao Liu[3], Yifan Wang[1], Rui Yang[1], Caihong Liu[1], Chang He[1], Anyu Wang[1], Lingfei Ma[1], Jinde Zhang[1], Wenbu Lu[4], Jiahao Li[1], Hao Li[1], Xing Han[5]*, Shan Liu[6]*, Cheng Jiang[1]*, Chen-zhong Li[1]*

hanx83@mail.sysu.edu.cn; shanliusyy@uestc.edu.cn; jiangcheng@cuhk.edu.cn; lichenzhong@cuhk.edu.cn

**The file includes:**

Materials and Methods
Supplementary Text
Figs. S1 to S33
Tables S1 to S2

**Other Supplementary Materials for this manuscript include the following:**

Movies S1 to S2

## Materials and Methods

### Ethical statement

All animal procedures were reviewed and approved by the Animal Management Committee of The Chinese University of Hong Kong, Shenzhen (Approval No. CUHKSZ-D-20250007). All experiments were performed in accordance with institutional guidelines and the National Research Council's Guide for the Care and Use of Laboratory Animals. Animals were housed under standard laboratory conditions with controlled temperature, humidity, and light/dark cycles, and all efforts were made to minimize animal discomfort and the number of animals used.

### Materials

Poly(3,4-ethylenedioxythiophene): poly(styrenesulfonate) (PEDOT: PSS) aqueous dispersion was purchased from Clevios, Germany. 1-Ethyl-3-(3-dimethylaminopropyl) carbodiimide hydrochloride (EDC), N-hydroxysuccinimide (NHS), and dopamine hydrochloride (DA·HCl) were obtained from Aladdin Co., Ltd. (Shanghai, China). Hyaluronic acid (HA; molecular weight, 500–700 kDa) and poly-L-lysine (PLL; molecular weight, 2–5 kDa) were purchased from Bloomage Biotechnology Co., Ltd. (Jinan, China). Sodium bis(2-ethylhexyl) sulfosuccinate (AOT), isooctane, lithium bromide, sodium hydroxide, carbon nanotubes, graphene, dimethyl sulfoxide (DMSO), thiol-terminated polyethylene glycol (PEG-SH), carboxyl-terminated polyethylene glycol (PEG-COOH), and azide-terminated polyethylene glycol (PEG-$N_3$) were purchased from Sigma-Aldrich, USA. Unless otherwise stated, all other chemicals were purchased from Aladdin Co., Ltd. and used as received. Deionized water was used throughout all experiments.

### Statistical analysis

All quantitative data are presented as mean ± standard deviation unless otherwise stated. Statistical analyses were performed using one-way analysis of variance for comparisons among multiple groups. When appropriate, post hoc tests were used for pairwise comparisons. Statistical significance was defined as $P < 0.05$. Significance levels are indicated as follows: *$P < 0.05$, **$P < 0.01$, ***$P < 0.001$. The number of biological or technical replicates is indicated in the relevant figure legends or experimental descriptions.

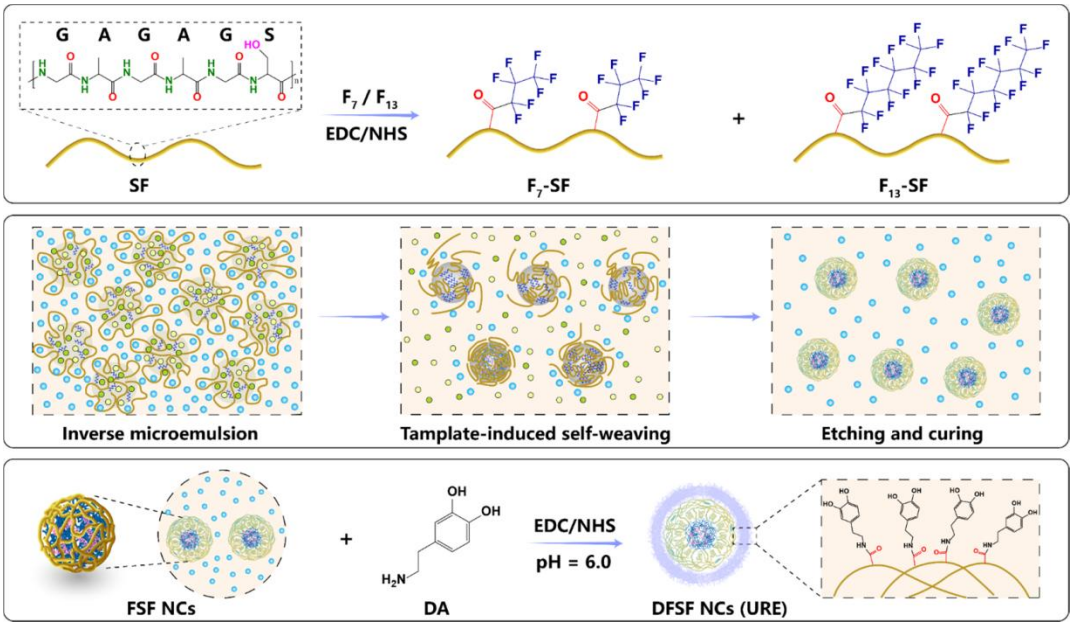



**Fig. S1.** Schematic illustration of silk fibroin fluorination, fabrication of hollow nanocage-structured ultrasound-responsive elements (UREs) via self-weaving technology, and subsequent surface modification of UREs with dopamine (DA).

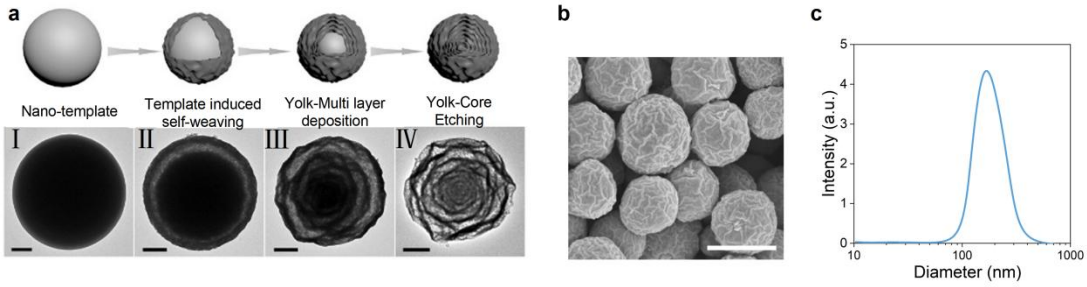



**Fig. S2. Characterization of URE fabrication.** (a) Schematic detailing the mechanism of the self-weaving fabrication process for UREs. (b) Scanning electron microscopy (SEM) image of UREs. (c) Diameter distribution of UREs determined by dynamic light scattering (DLS).

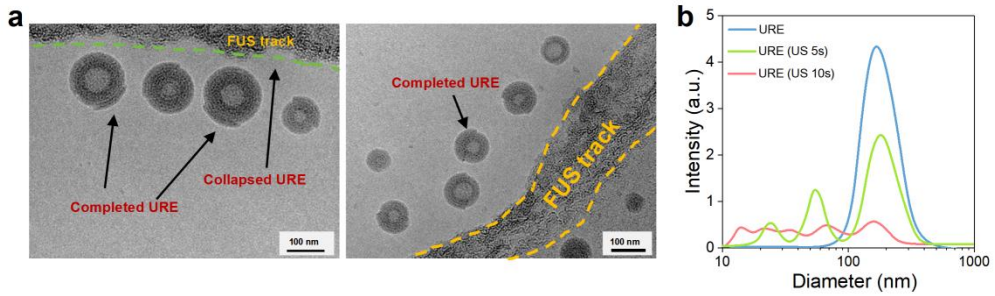



**Fig. S3. Structural response of UREs to focused ultrasound (FUS)**. (a) Transmission electron microscopy (TEM) image of UREs treated with focused ultrasound (FUS); the FUS treatment track is clearly visible. (b) Monitoring of URE diameter changes following FUS treatment for varying irradiation times.

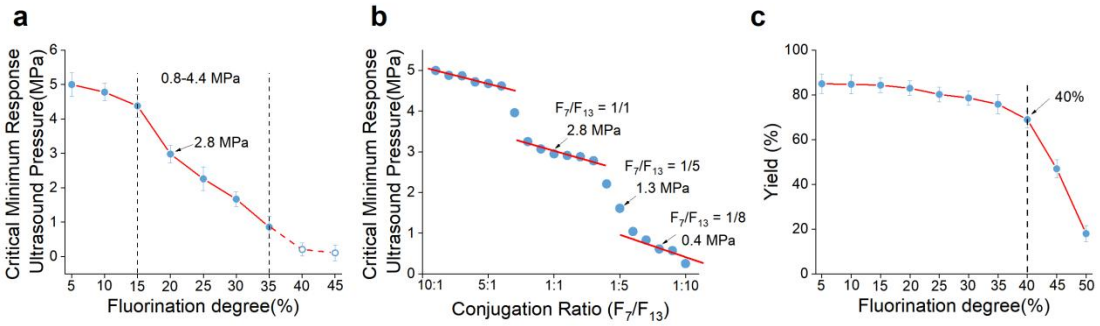



**Fig. S4. Optimization of URE fluorination degree.** (a) Evaluation of the critical buckling pressure of UREs with varying degrees of fluorination. (b) Calibration of the critical buckling pressure of UREs. (c) Fabrication yield of UREs as a function of the degree of fluorination.

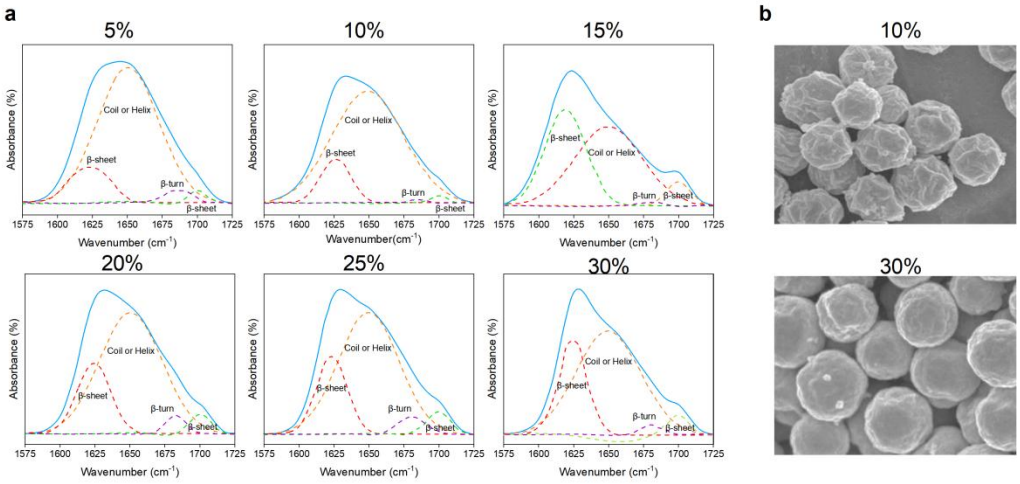
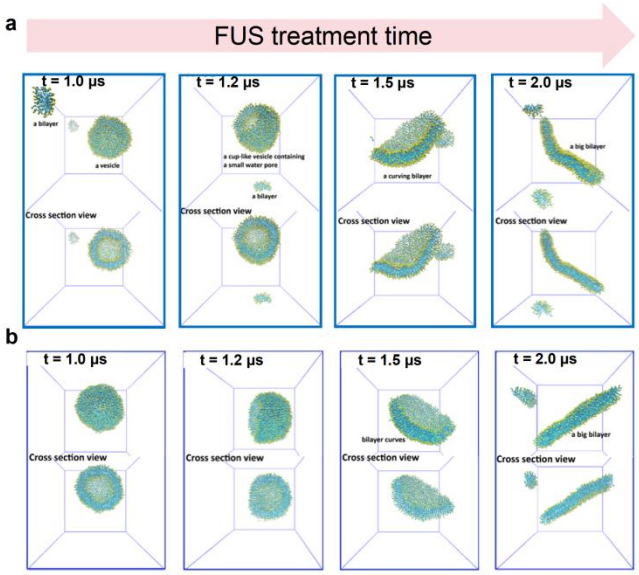


**Fig. S5. Effect of fluorination degree on URE structure and morphology.** (a) Raman spectroscopy of UREs with varying degrees of fluorination, alongside a deconvolution analysis of the secondary structures (β-sheet, β-turn, and α-helix) of silk fibroin within the UREs. (b) SEM images of UREs with different fluorination degrees, demonstrating the impact of fluorination on the surface profile, which directly correlates with the critical buckling pressure.



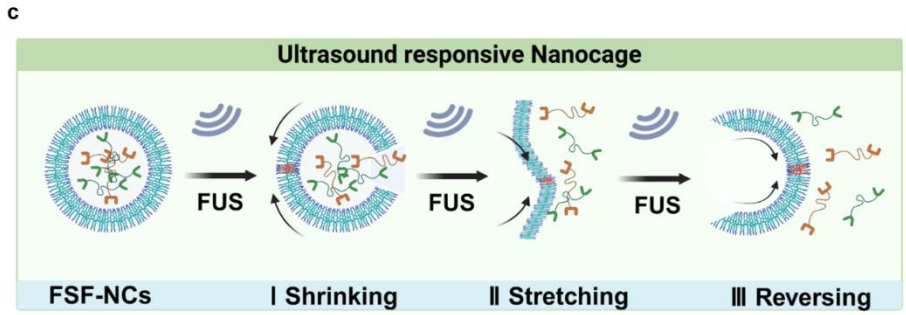




**Fig. S6. Molecular dynamics simulation of URE responsiveness to ultrasound.** (a) Molecular dynamics (MD) analysis of structural changes in UREs upon ultrasound stimulation. (b) Replicate results of MD simulations demonstrating URE responsiveness to ultrasound. (c) Schematic illustrating the underlying mechanism of URE responsiveness to ultrasound stimulation.

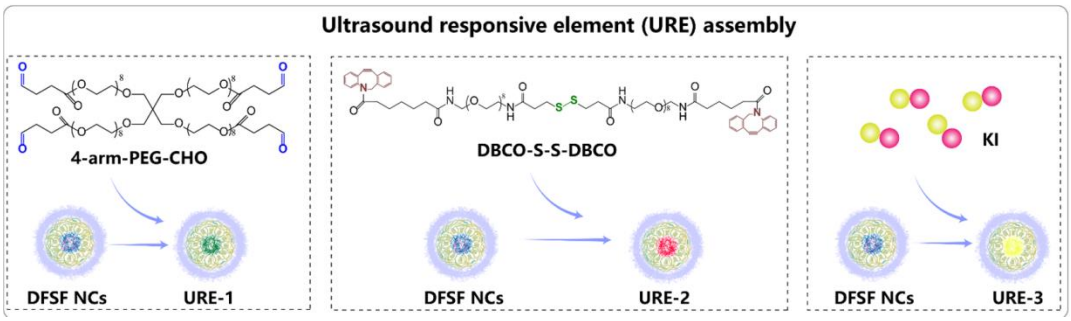



**Fig. S7. Schematic illustration of URE assembly.** URE-1 is loaded with 4-arm-PEG-CHO as crosslinker A; URE-2 is loaded with DBCO-S-S-DBCO as crosslinker B; and URE-3 is loaded with potassium iodide (KI) as crosslinker C, which accelerates disulfide bond formation.

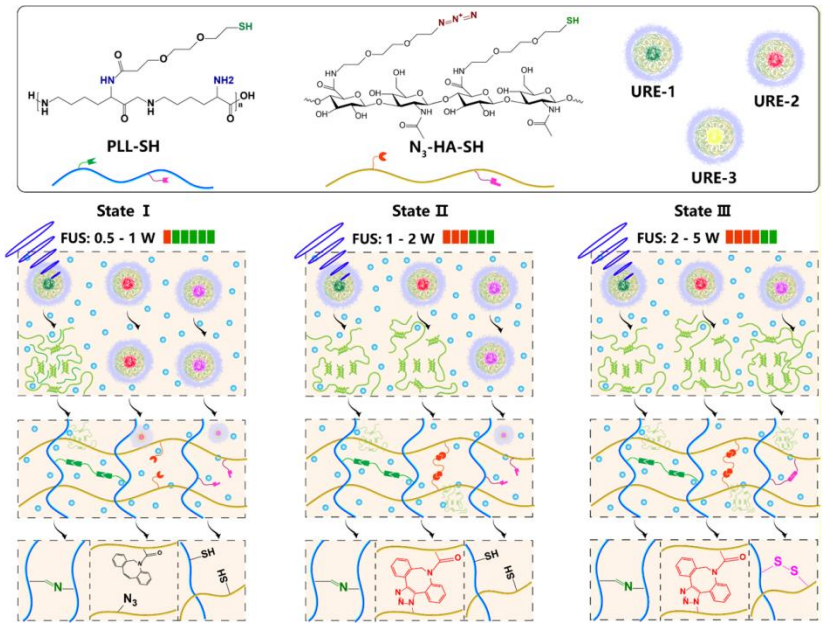



**Fig. S8. Schematic illustration of the modular US-Ink system.** The US-Ink consists of specifically modified polymer chains as the substrate, UREs as ultrasound-responsive elements, and functional dopants. The lower panel illustrates the crosslinking mechanism of US-Ink after FUS treatment and the programmable responsiveness regulated by ultrasound pressure. This programmable process involves three sequential and selective steps: URE activation, crosslinker release, and localized US-Ink crosslinking.

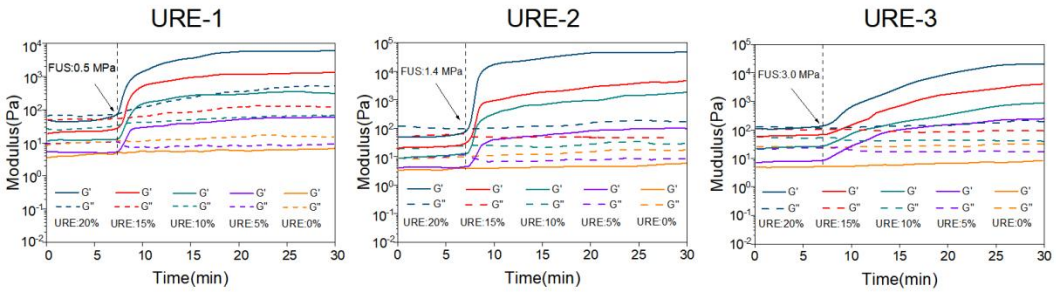



**Fig. S9. Rheological characterization of US-Ink crosslinking behavior.** The analysis evaluates the response sensitivity of different URE types and the mechanical properties of US-Ink formulations with varying URE concentrations.

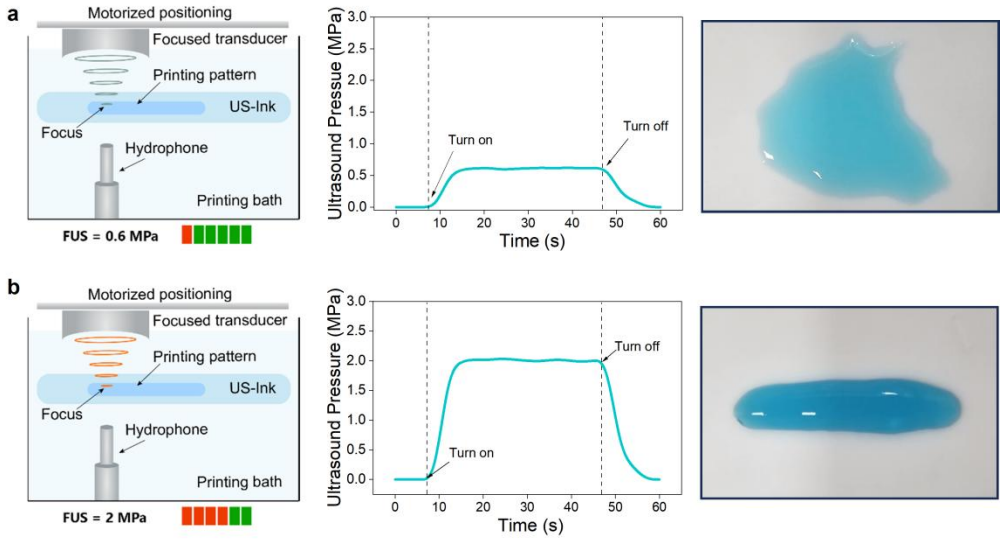



**Fig. S10. In vitro validation of US-Ink printing using FUS at a frequency of 1.88 MHz and a power of 3 W.** The left panel shows the printing setup, in which a focused transducer is controlled by a motorized positioning system; a hydrophone was used to map the ultrasound field distribution. Printing fails at an ultrasound pressure of 0.4 MPa, whereas designed US-Ink patterns are successfully printed at 2.0 MPa. The middle panel shows the ultrasound pressure distribution at the focal point during printing. The right panel shows representative images of failed and successful US-Ink printing.

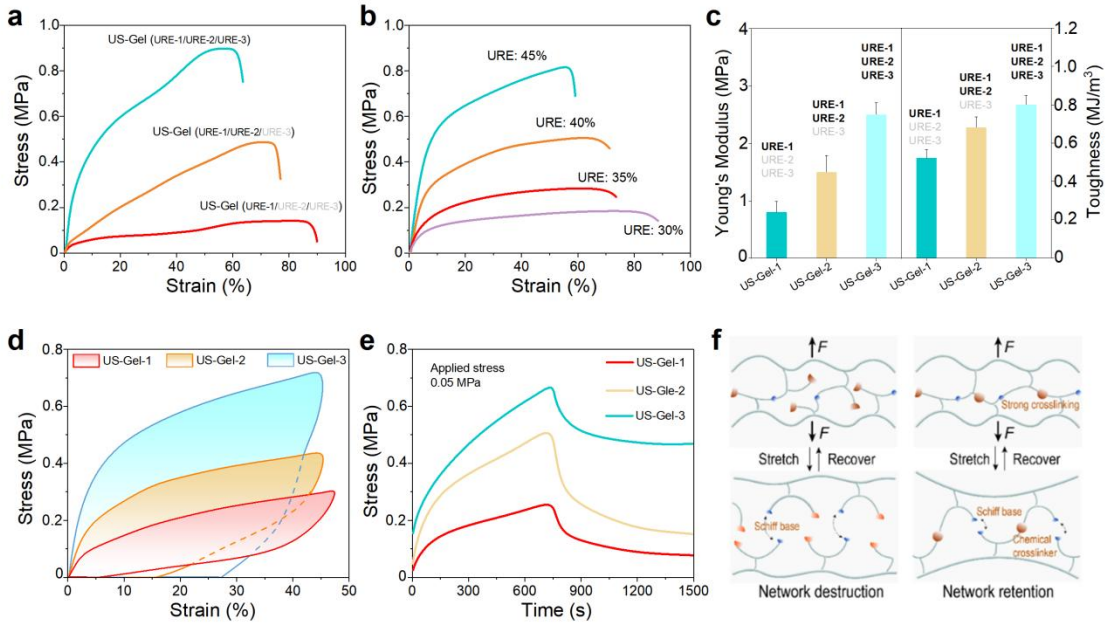



**Fig. S11. Mechanical characterization of printed US-gels.** (a) Mechanical properties of US-gels printed by FUS at different ultrasound pressures: 0.5 MPa, 1.4 MPa, and 3.0 MPa, corresponding to the activation of URE-1 alone, URE-1 plus URE-2, and URE-1 plus URE-2 plus URE-3, respectively. (b) Mechanical properties of printed US-gels at various URE concentrations. (c) Analysis of Young's modulus and toughness based on the data in (a). (d) Cyclic tensile testing of printed US-gels containing different URE types. (e) Stress relaxation tests of printed US-gels containing different URE types. (f) Schematic illustrating the self-healing mechanism and the reversible dynamic alterations of the crosslinking network in the printed US-gel within a specific force range.

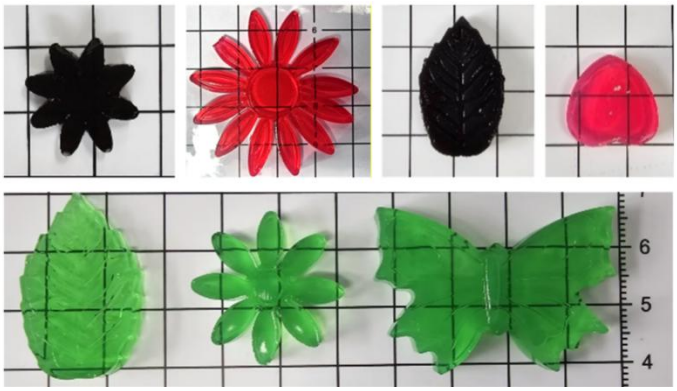


**Fig. S12.** Photographs of US-Ink printed into various configurations, including English letters and complex patterns, using different polymer or dye dopants.

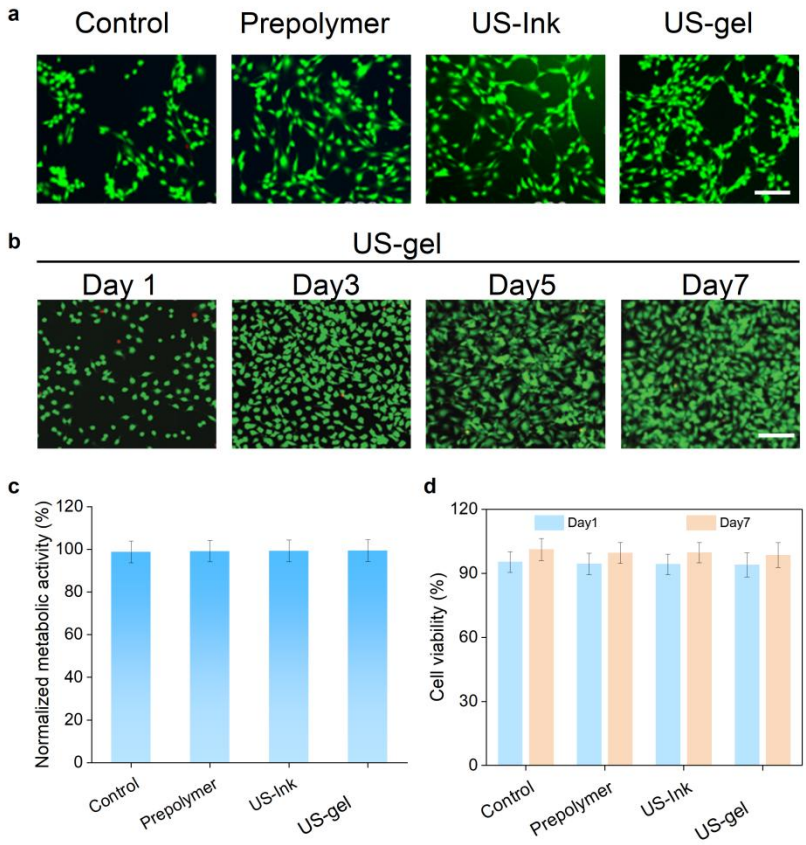



**Fig. S13. In vitro biocompatibility of US-Ink and US-gel**. (a) Live/dead staining images of cells on day 2 after exposure to different samples. (b) Live/dead cell staining images of cells exposed to US-gel over varying culture periods. Scale bars:100μm. Human dermal fibroblasts (HDFs) were utilized in this experiment. (c-d) Viability of HDFs corresponding to the conditions in (A) and (B), respectively (n = 3).

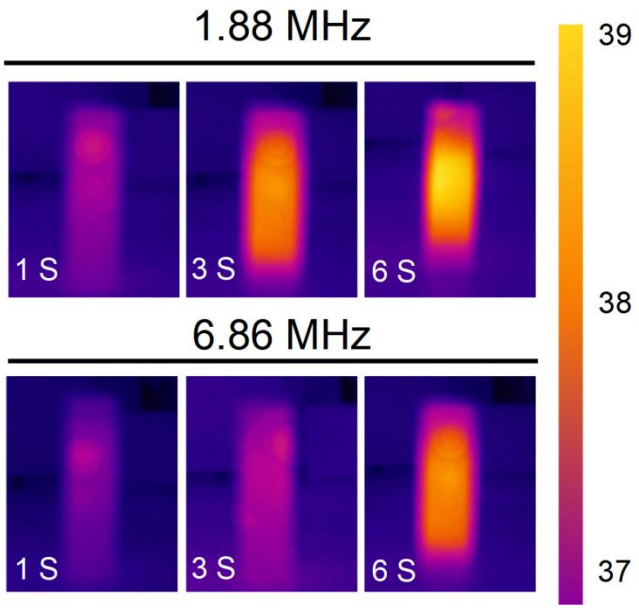



**Fig. S14.** Infrared thermal imaging of US-Ink treated with FUS for different durations to evaluate temperature changes during the printing process. Two transducers with different operating frequencies were utilized for this assessment.

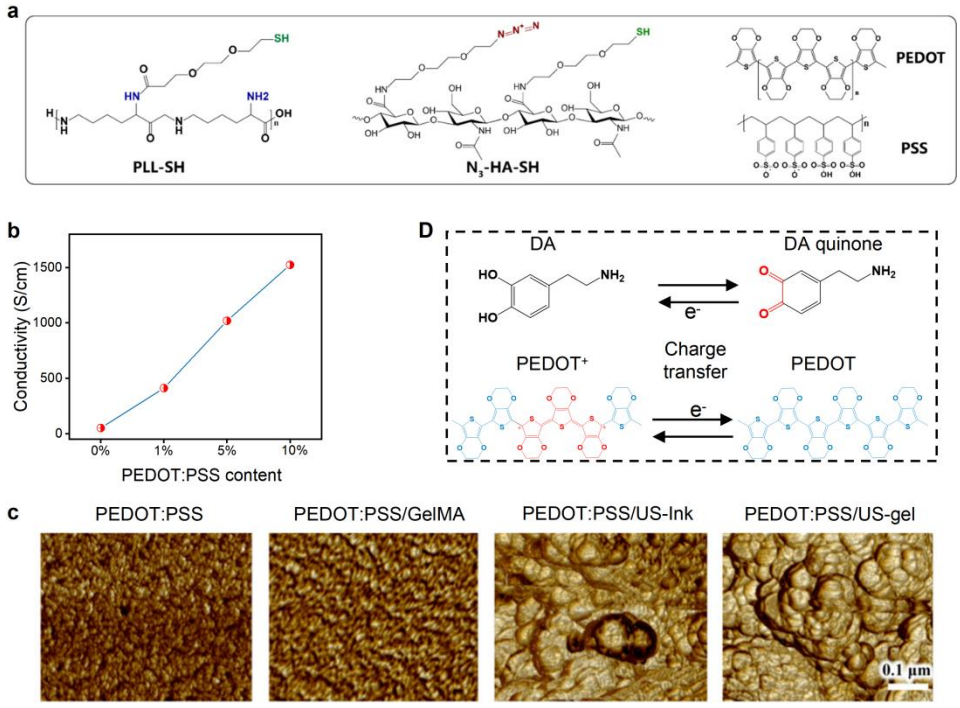



**Fig. S15. Electrical conductivity of printed US-gels.** (a) Schematic depicting the formulation of the conductive US-Ink containing PEDOT:PSS as a conductive polymer dopant . (b) Conductivity of the printed US-gel at different PEDOT: PSS concentrations. (c) Atomic force

microscopy (AFM) images revealing the phase-separated blocks of PEDOT: PSS within the US-gel. (d) Schematic illustration of the mechanism by which DA modification on the URE surface enhances charge transfer, thereby significantly increasing the overall conductivity of the US-gel.

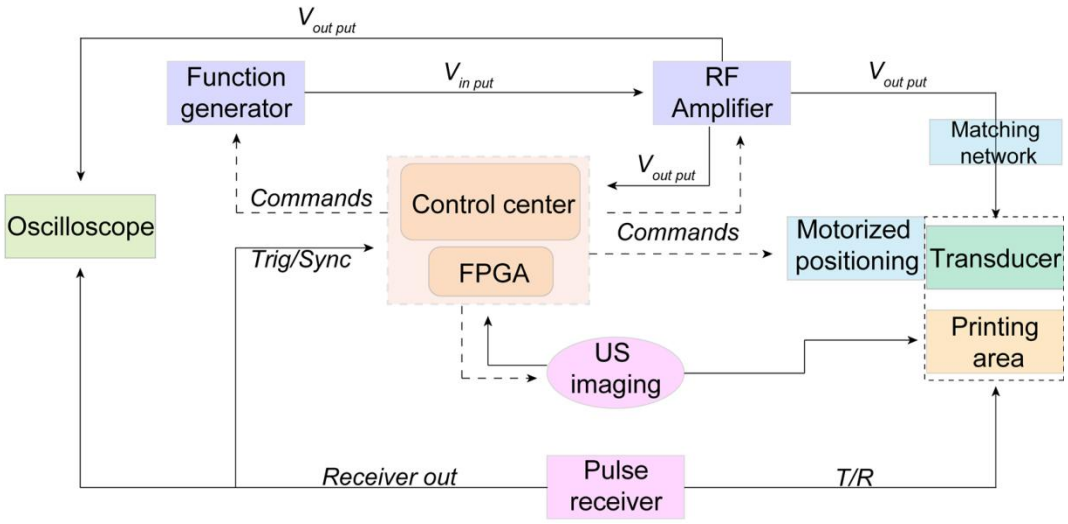



**Fig. S16.** Schematic of the ultrasound printing setup for FUS generation, monitoring, and control. RF: radio frequency; T/R: transmitter/receiver.

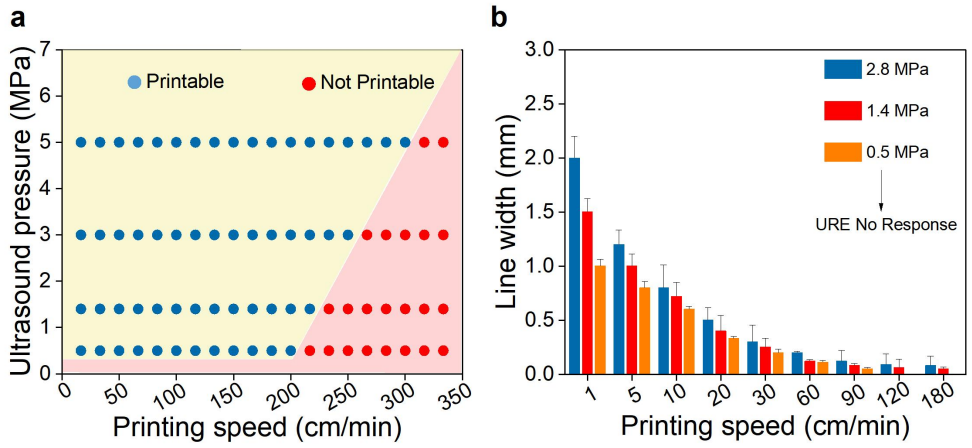



**Fig. S17. Printability and printing resolution of US-Ink using a 4.25 MHz transducer.** (a) Printability of the US-Ink at different power levels and printing speeds. (b) Printing resolution of US-Ink at different ultrasound pressures and printing speeds.

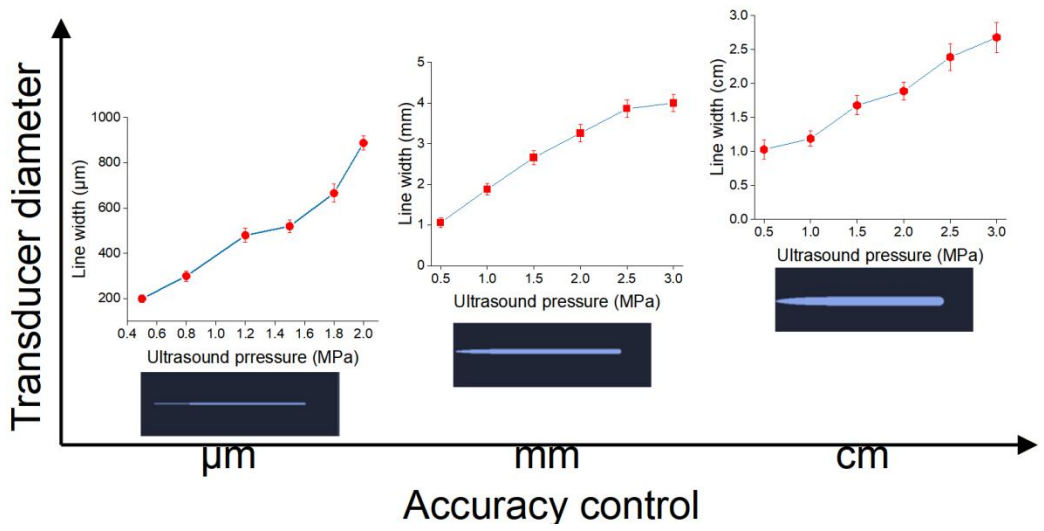



**Fig. S18.** Detailed evaluation of printing resolution using FUS transducers of various diameters. The printing resolution, defined by the printed line width, scales from the micrometer to the centimeter level in accordance with the transducer diameter.

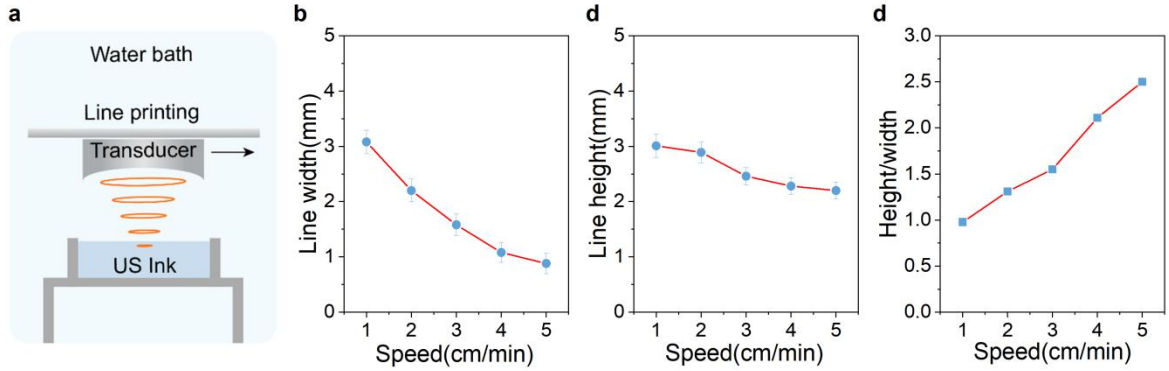



**Fig. S19. Printing resolution within a 5 mm US-Ink tank.** (a) Schematic of the in vitro setup positioned beneath the US-Ink tank. Lateral (b) and axial (c) resolutions of lines printed at various speeds using a 1.88 MHz transducer. (d) Longitudinal resolution of the US-Ink printed at various speeds. Error bars represent the standard deviation of the mean (n = 4).

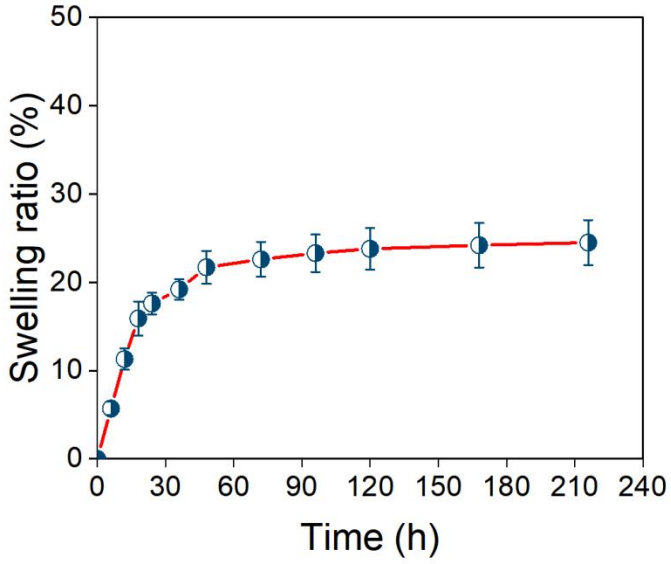



**Fig. S20.** Swelling ratio of the printed US-gel, measured in phosphate-buffered saline (PBS).

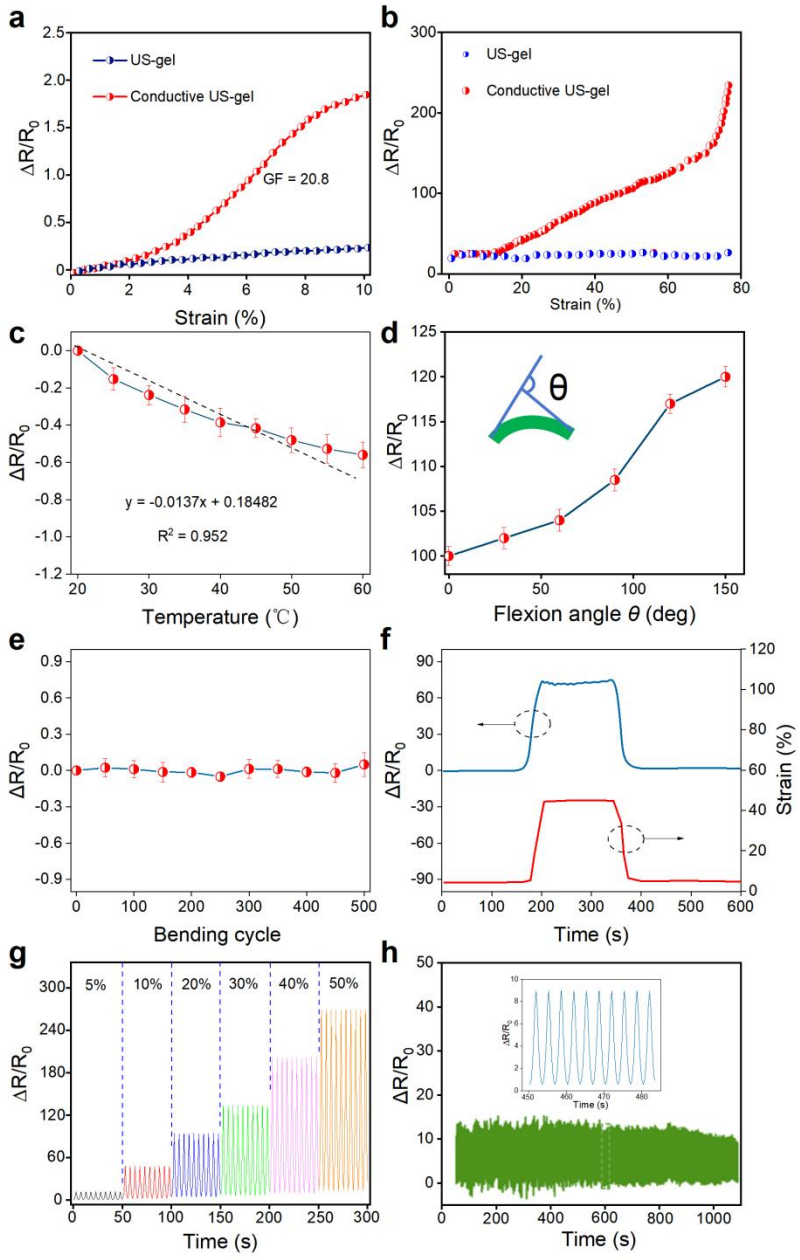



**Fig. S21. In vitro characterization of the printed US-gel strain sensor.** (a) Resistance response and gauge factor (GF) of the sensor during 0 – 10% stretching. (b) Resistance response and GF of the sensor under 0 – 80% strain. (c) Resistance response of the printed sensor at different testing temperatures. (d) Resistance response of the printed sensor at various flexion angles. (e) Resistance changes of the printed sensor across multiple bending cycles. (f) Response speed of the strain sensor during loading and unloading phases. (g) Resistance response of the sensor unit under 5% to 50% applied strain. (h) Resistance response of the sensor unit over 1,000 stretch-release cycles at 10% strain increments.

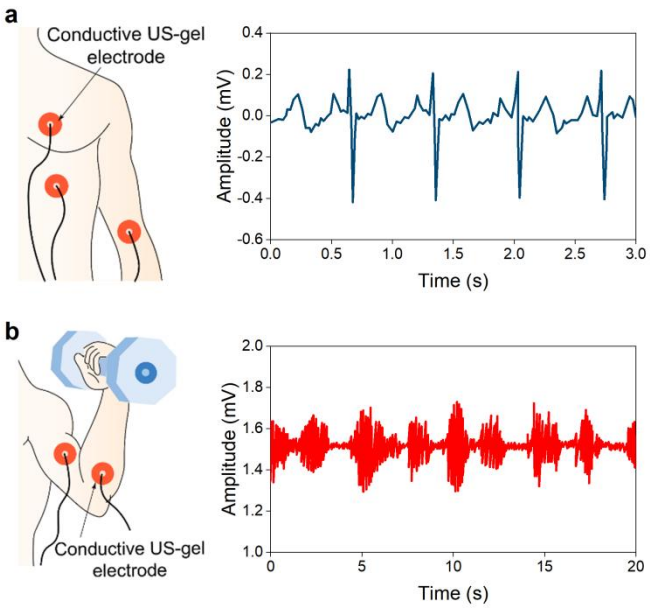



**Fig. S22. AiUP-printed conductive US-gel strain sensors used for recording human electrophysiological signals.** (a) electrocardiogram (ECG) and (b) electromyogram (EMG) recordings in a human volunteer.

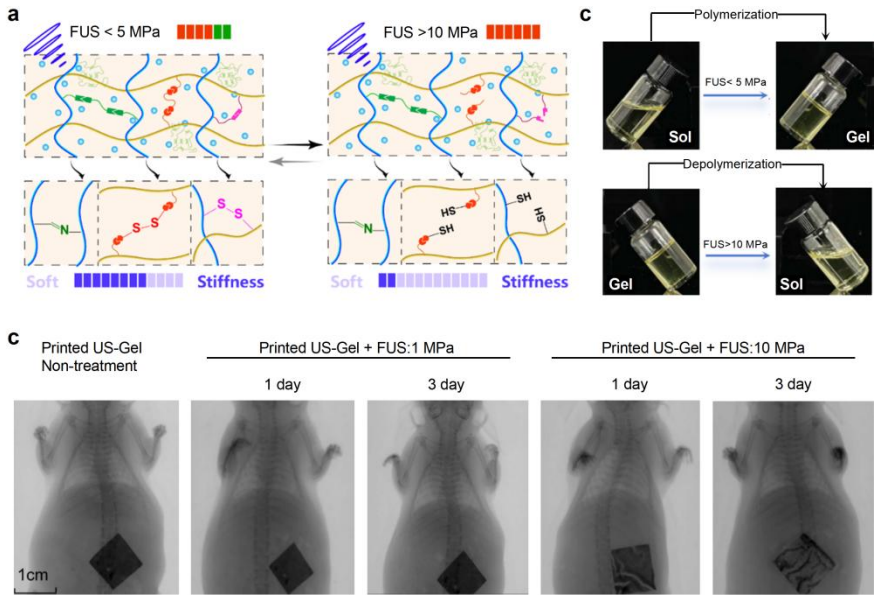



**Fig. S23. Ultrasound-controlled degradation of printed electrodes.** (a) Schematic detailing the distinct ultrasound pressure thresholds required for US-Ink printing versus US-gel degradation. (b) Photographs demonstrating the targeted polymerization of US-Ink and depolymerization of the US-gel under different applied ultrasound pressure thresholds. (c) In vivo evaluation of the ultrasound pressure-controlled degradation of the printed US-gel.

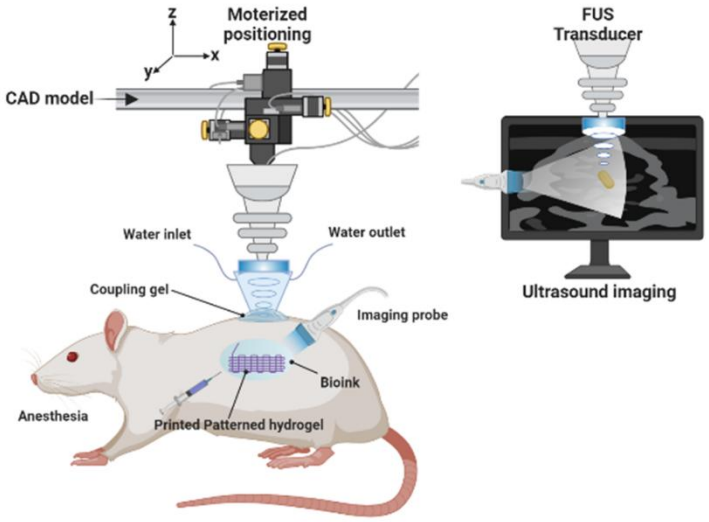



**Fig. S24.** In vivo AiUP setup in live animal models, employing AI-controlled closed-loop manipulation for precise printing.

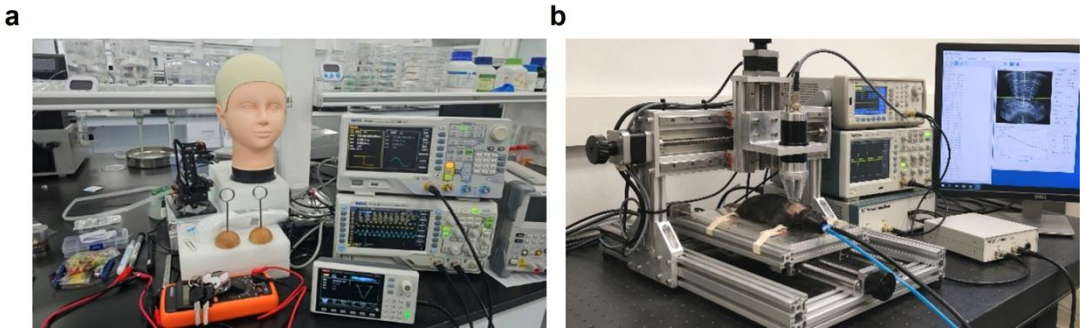



**Fig. S25.** Photographs of the AiUP setup for (a) in vitro printing and (b) in vivo printing applications.

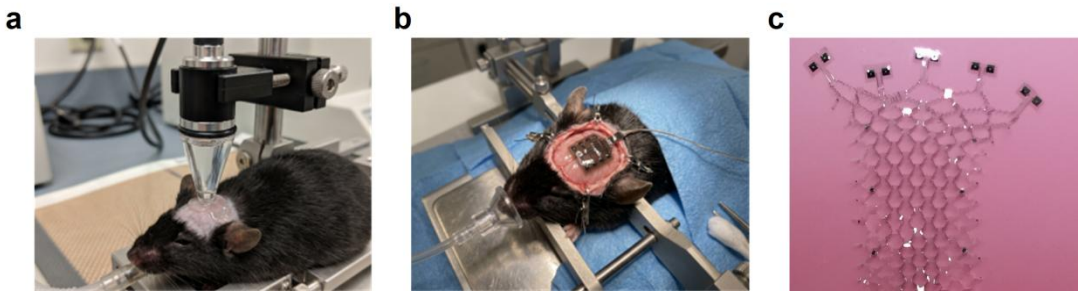



**Fig. S26. Fabrication and handling of a cortical electrode using AiUP.** (a) the AiUP printing process, (b) observation through a craniotomy window, and (c) peeling-off of the printed electrode.

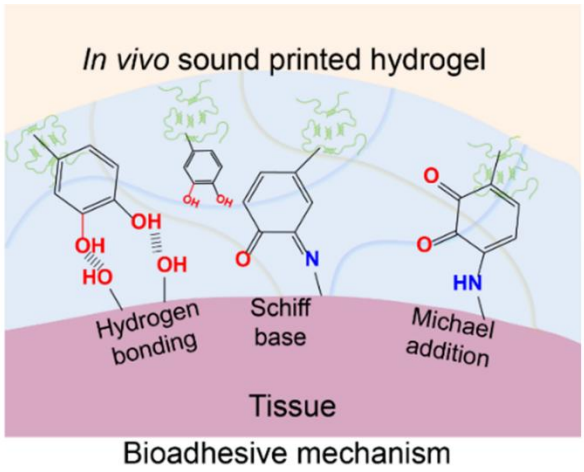



**Fig. S27.** Schematic illustration of the adhesion mechanism by which the printed US-gel electrode achieves strong attachment to target tissues.

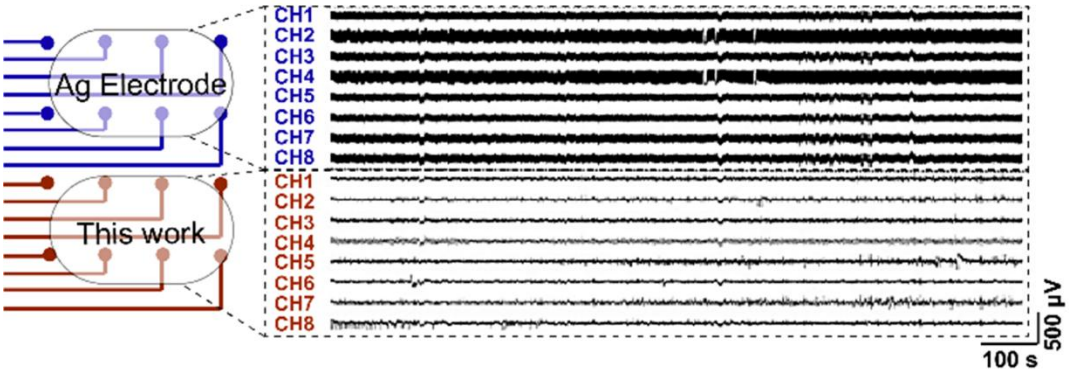



**Fig. S28.** Comparison of local field potential (LFP) signals recorded using standard Ag electrodes versus the printed US-gel electrodes developed in this study.

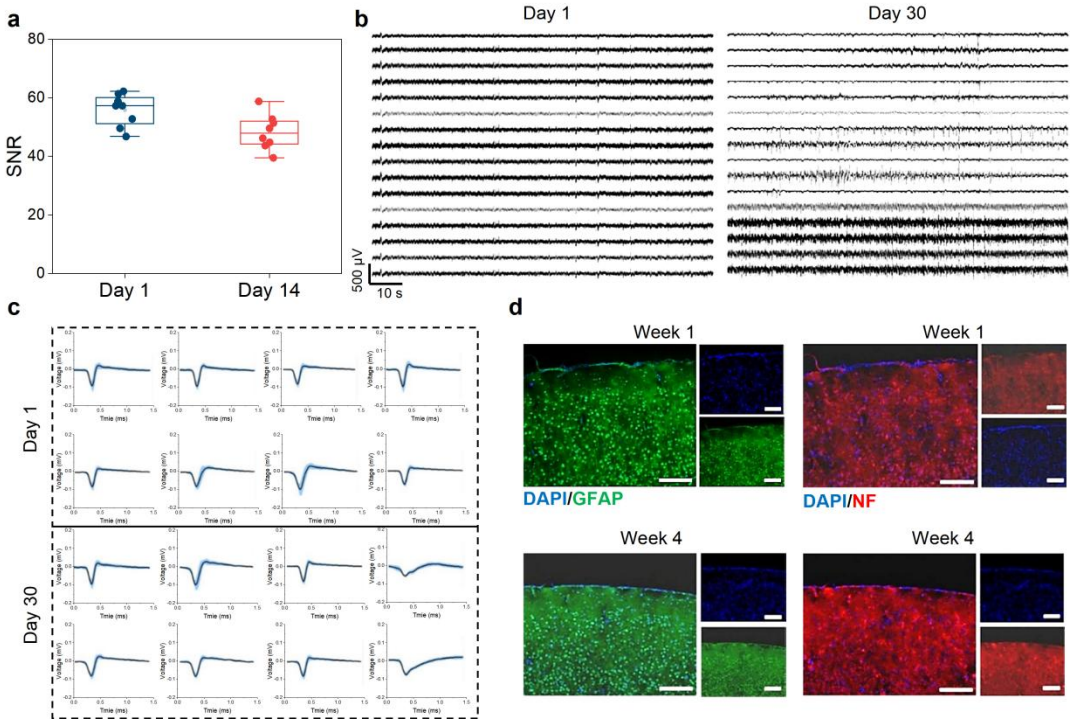



**Fig. S29. In vivo performance and biocompatibility of the printed 8-channel cortical electrode.** (a) Signal-to-noise ratios (SNRs) of LFP signals detected on day 1 and day 14 after printing. (b) Representative LFP signals recorded on day 1 and day 14. (c) Neural spikes captured by the printed electrode on day 1 and day 14. (d) Immunofluorescence images of brain slices collected 1 week and 4 weeks after printing the 8-channel cortical electrode. Untreated brain slices were used as controls. GFAP, glial fibrillary acidic protein, used as an astrocyte/glial marker; NF, neurofilament, used as a neuronal marker.

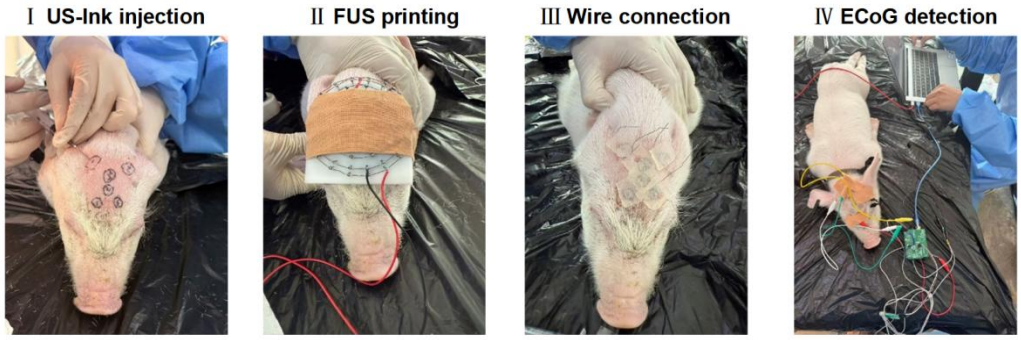



**Fig. S30.** Photographs showing the AiUP printing process in a minipig model, including US-Ink injection, FUS printing, wire connection, and subsequent electrocorticography (ECoG) recording.

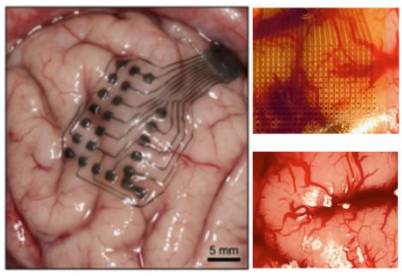



**Fig. S31.** Photograph of the cortical electrode printed via AiUP in a Bama pig model.

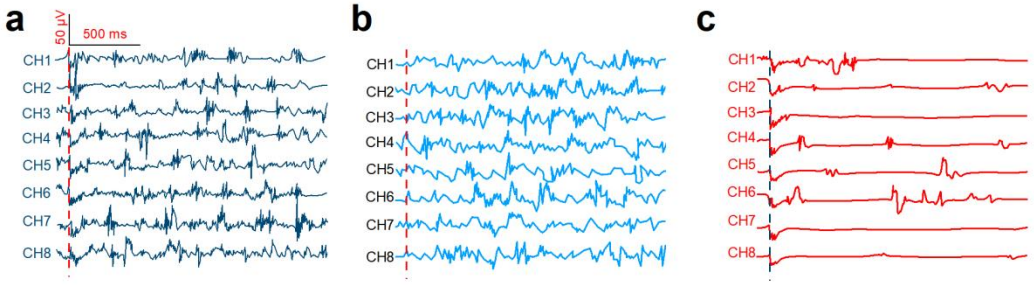



**Fig. S32.** (a) ECoG traces recorded from printed electrodes during tactile stimulation of the rostrum. (b) ECoG traces recorded under behavioral anesthesia. (c) ECoG traces recorded under light anesthesia.

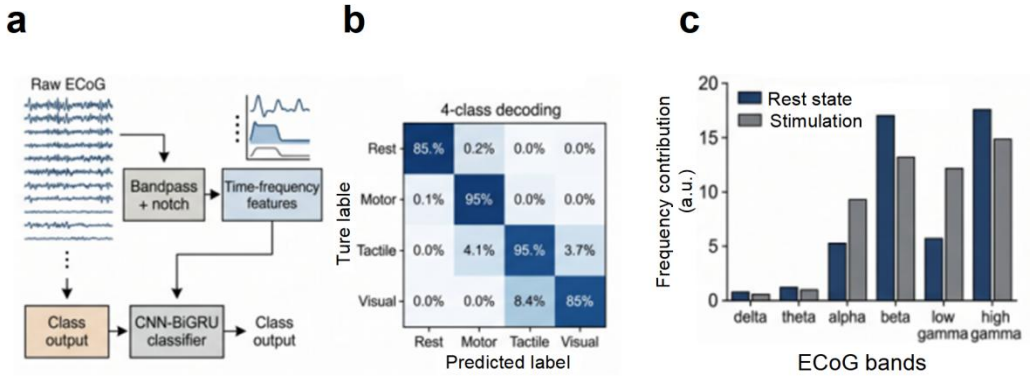



**Fig. S33**. (a) Preprocessing and convolutional recurrent neural network architecture for ECoG decoding. Raw signals were down sampled to 1 kHz and processed to extract low-frequency and high-gamma neural features. Features were fed into a convolutional recurrent neural network consisting of a one-dimensional convolutional layer, bidirectional gated recurrent units, and a fully connected layer. (b) Decoding accuracy under different experimental conditions in pigs. (c) Classification of ECoG signals recorded by printed electrodes across experimental states

**Table S1.**

URE formulations, corresponding acoustic response thresholds, US-Ink formulations, and gelation times.

| **URE formulation** (Fluor. Deg.) | Acoustic response thresholds (MPa) | **US-Ink formulation** (URE ratio) | Gelation time (s) |
|---|---|---|---|
| 42% | 0.2 | 5% | 300 |
| **40%** | **0.4** | 10% | 180 |
| 38% | 0.5 | 18% | 150 |
| 35% | 0.8 | 20% | 120 |
| **32%** | **1.3** | 22% | 100 |
| 30% | 1.5 | 25% | 80 |
| 25% | 2.1 | 28% | 60 |
| **20%** | **2.8** | 30% | 40 |
| 18% | 3.0 | 35% | 20 |

Noted: Values highlighted in bold indicate formulations selected for in vivo electrode printing.

**Table S2.**

Summary of AiUP printing parameters used in this study.

| Ultrasound parameters | Printing speed (cm/min) | Printing depth (cm) | EchoAgent using | Printing type |
|---|---|---|---|---|
| Freq. 1.88 MHz | | 1 | Y | *In vivo* electrode |
| Power. 2 W | 5 cm/min | 1 | N | *In vivo* electrode |
| Pres. 0.5 MPa | | 2 | Y | *In vitro* pattern |
| Freq. 1.88 MHz | | 1 | Y | *In vivo* electrode |
| Power. 5 W | 20 cm/min | 1 | N | *In vivo* electrode |
| Pres. 1.4 MPa | | 2 | Y | *In vitro* pattern |
| Freq. 1.88 MHz | | 1 | Y | *In vivo* electrode |
| Power. 8 W | 60 cm/min | 3 | N | *In vitro* pattern |
| Pres. 3.0 MPa | | 5 | Y | *In vitro* pattern |
| Freq. 2.74 MHz | | 1 | Y | *In vivo* electrode |
| Power. 3 W | 10 cm/min | 1 | N | *In vivo* electrode |
| Pres. 0.5 MPa | | 2 | Y | *In vitro* pattern |
| Freq. 2.75 MHz | 20 cm/min | 1 | Y | *In vivo* electrode |

| | | | | |
|---|---|---|---|---|
| Power. 10 W | | 1 | N | *In vivo* electrode |
| Pres. 2.8 MPa | | 2 | Y | *In vitro* pattern |
| Freq. 6.86 MHz | | 1 | Y | *In vivo* electrode |
| Power. 6 W | 5 cm/min | 1 | N | *In vivo* electrode |
| Pres. 0.5 MPa | | 2 | Y | *In vitro* pattern |
| Freq. 6.86 MHz | | 1 | Y | *In vivo* electrode |
| Power. 10 W | 10 cm/min | 1 | N | *In vivo* electrode |
| Pres. 2.5 MPa | | 2 | Y | *In vitro* pattern |

Note: Y, yes; N, no.

**Movie S1.**

In vivo ultrasound printing in a live Bama pig. A cortical electrode was printed using AiUP in a live pig model for ECoG signal detection and pig ECoG decoding.

**Movie S2.**

AiUP printed electrode recording the ECoG on mice and detecting the epilepsy signaling on a mouse epilepsy model.